



Geophysical Research Letters



RESEARCH LETTER

10.1029/2023GL106181

Key Points:

- We present the first mapping of the grounding line of Jakobshavn Isbr\$\ae \$, Greenland at ocean tidal frequencies
- The grounding line migrates over kilometers, far more than expected from flotation, which we attribute to kilometer-size seawater intrusions
- Seawater intrusions along a bed several hundred meters deeper than expected must be included in future glacier modeling studies

Supporting Information:

Supporting Information may be found in the online version of this article.

Correspondence to:

J. H. Kim, jaehuk2@uci.edu

Citation:

Kim, J. H., Rignot, E., Holland, D., & Holland, D. (2024). Seawater intrusion at the grounding line of Jakobshavn Isbræ, Greenland, from terrestrial radar interferometry. *Geophysical Research Letters*, *51*, e2023GL106181. https://doi.org/10.1029/2023GL106181

Received 7 SEP 2023 Accepted 11 MAR 2024

© 2024. The Authors. This is an open access article under the terms of the Creative Commons Attribution-NonCommercial-NoDerivs License, which permits use and distribution in any medium, provided the original work is properly cited, the use is non-commercial and no modifications or adaptations are made.

Seawater Intrusion at the Grounding Line of Jakobshavn Isbræ, Greenland, From Terrestrial Radar Interferometry

Jae Hun Kim¹, Eric Rignot^{1,2,3}, David Holland^{4,5}, and Denise Holland^{4,5}

¹Department Earth System Science, University of California Irvine, Irvine, CA, USA, ²Jet Propulsion Laboratory, California Institute of Technology, Pasadena, CA, USA, ³Department Civil and Environmental Engineering, University of California Irvine, Irvine, CA, USA, ⁴Center for Global Sea Level Change, New York University Abu Dhabi, Abu Dhabi, UAE, ⁵Courant Institute of Mathematical Sciences, New York University, New York, NY, USA

Abstract Jakobshavn Isbræ, a major outlet glacier in Greenland, lost its protective ice shelf in 2002 and has been speeding up and retreating since. We image its grounding line for the first time with a terrestrial radar interferometer deployed in 2016 and detect its migration at tidal frequencies. The southern half of the glacier develops a floating section $(3 \text{ km} \times 3 \text{ km})$ that migrates in phase with the tidal difference, up to a distance of 2.8 km, far more than previously expected. We attribute the migration to kilometer-scale seawater intrusions, 10-20 cm in height, with the tide. The intrusions reveal that the glacier bed may be up to 800 m deeper than expected on the south side, which illustrates that our knowledge of bed topography remains limited for this glacier. We expect seawater intrusions to cause rapid melt of basal ice and play a major role in the glacier evolution.

Plain Language Summary The transition boundary between grounded glacier ice and floating glacier ice, or grounding line, has never been mapped in much detail on the largest, fastest outlet glaciers of Greenland because available satellite radar imagery does not provide short enough repeat pass data. Here, we use a terrestrial radar interferometer which images the glacier every 2 min to map the grounding line repeatedly with differential interferometry. Surprisingly the glacier develops a small floating section on the south side where the grounding line migrates over considerable distances—0.5 to 2.8 km—during the tidal cycle, which is 10 times farther than previously expected from flotation. We attribute the migration to seawater intrusions over a bed 100–800 m deeper than previously known. Seawater intrusions will carry sufficient ocean heat to melt basal ice vigorously, a factor that has not been incorporated in modeling studies of this glacier.

1. Introduction

The contribution to sea level rise from the Greenland Ice Sheet has increased significantly in the past decades due to the accelerated flow of its glaciers and the enhanced melting of its snow and ice surface (Mouginot, Rignot, et al., 2019). Jakobshavn Isbræ(JI, Sermeq Kujalleq), in West Greenland, is the largest and fastest moving outlet glacier in Greenland; it drains 6.5% of the ice-sheet area (Joughin et al., 2004). Repeated laser-altimeter surveys by NASA's Airborne Topographic Mapper since 1991 have shown that the glacier experienced a slight thickening in the lower reaches between 1991 and 1997 at 10 cm/yr, before thinning after 1997 with rates exceeding 15 m/yr (Thomas, 2004). The glacier floating ice tongue collapsed in 2002, followed by a tripling in ice speed at its terminus (Joughin et al., 2004) which remains its present-day speed (Khazendar et al., 2019). The retreat has been attributed to the incursion of warm ocean waters of sub-tropical origin in Ilullisat fjord in the mid 1990s (Holland et al., 2008), which resulted in high rates of ice shelf melt (Thomas, 2004). During the retreat, the glacier thinned at rates up to 30 m/yr (Thomas et al., 2009), which contributed to more retreat as the glacier reached flotation sooner.

It has been assumed that once the glacier lost its ice shelf in 2002, only a small section of the glacier front was afloat (Rosenau et al., 2013). While the imaging of a glacier grounding line is possible with satellite radar interferometry (Rignot et al., 2011), this has only been done once using ERS-1 Synthetic Aperture Radar (SAR) interferometry from year 1996, and has not been possible to repeat with any other SAR sensors since. Due to the high flow speed and deformation rate of JI, the repeat cycle of existing SAR satellites is too long to maintain phase coherence and avoid phase aliasing within image elements, that is, phase values change by more than one cycle within the elements. Other tools used to map the limit of ice flotation, for example, laser altimetry or radar depth sounding, are much less precise to pinpoint the location of the grounding line (Friedl et al., 2020).

KIM ET AL. 1 of 10

Another limitation is our knowledge of ice thickness and bed topography. JI is more than 1 km thick at its grounding line, with warm temperate ice near its bed (Clarke & Echelmeyer, 1996) that is highly absorptive of radar sounding signals. The warm ice base, coupled by strong side echoes from a deep trench in the bedrock, and high surface clutter from a broken-up surface, have made it challenging to measure ice thickness, despite multiple attempts over many decades with both high and low frequency airborne radar sounders (Leuschen et al., 2010, updated 2017). Farther upstream, radar echoes and seismic profiles have been successfully collected (Clarke & Echelmeyer, 1996). In the outer fjord, a shipborne survey took place in April 2021 as part of NASA's Earth Venture Mission "Ocean Melting Greenland" (Fenty et al., 2016). At the ice front, a high resolution airborne gravity survey from July 2012 was combined with discrete depth soundings from Conductivity, Temperature, Depth probes to produce a bed map, affected by residual uncertainties due to a lack of depth data near the ice front (An et al., 2017).

Here, we present an analysis of the front of JI using a terrestrial radar interferometer (Gamma Portable Radar Interferometer, GPRI) deployed on the southern side in June 2016 with a repeat cycle of 2 min. We use the data to detect the glacier grounding line and how it migrates, in near real time, during the tidal cycle. We present an interpretation of the results and discuss their implications for the evolution of the glacier in a warmer climate and its contribution to sea level rise.

2. Data and Methods

2.1. Terrestrial Radar Interferometry

The GPRI is a real-aperture radar operating at Ku-band (frequency 17.2 GHz) with a range resolution of 0.75 m. The GPRI scans the glacier every 2 min with a 170° scanning arc. The azimuth angle step is 0.2°, so the azimuth spacing varies with the distance from the radar from 7 m at 2 km range to 14 m at 4 km range. The total range of the instrument is 16.9 km (Werner et al., 2008).

The GPRI has one transmitting antenna and two receiving antennas mounted on a rotational scanner and separated by a baseline of 25 cm to measure surface topography in a single pass. In a repeat pass mode, GPRI combines results from one of the receiving antennas to measure the ground motion along the line of sight of the radar. Because the radar data are acquired at a low grazing angle (i.e., the GPRI sits 200 m above sea level and looking over a range of 5–15 km), parts of the glacier are shadowed from the radar illumination, so the glacier coverage is incomplete. Using the phase data, GPRI has been used to measure glacier velocity with a precision of 0.05 m/day (Voytenko et al., 2015).

The data used herein were collected from June 7 to June 20, 2016 from the south margin (Figure 1a) (Xie et al., 2018). The instrument was installed on a metal station connected to the bedrock and protected by a radome to minimize the effects of weather. The distance between the instrument and the ice front was about 2–5 km.

2.2. Data Processing

The GPRI complex images in slant-range geometry (Figure S1 in Supporting Information S1) are combined to generate radar interferograms with 20 looks in range and 1 in azimuth. We geocode the data at a spacing of 30 m into an Earth-fixed grid. The pointing angle of the GPRI is estimated at the sub-degree level by adjusting image features in the geocoded data with a reference Landsat image. Phase unwrapping is conducted from a single stationary point on the glacier side margin in each interferogram. To smooth the grounding line positions (Figure 1e) along profile C–C' (Figure 3), we applied locally weighted scatterplot smoothing algorithms (Derkacheva et al., 2020).

2.3. Differential GPRI Interferometry

The motion in the line of sight of the radar translates into variations in phase of 360° for every change in electric pathlength equal to half the radar wavelength, here 1.74 cm, independent of the size of the image elements. By differencing two consecutive interferograms spanning the same time interval, we measure the differential motion of the glacier caused by changes in oceanic tides (Rignot, 1996), non-steady horizontal flow, or changes in subglacial hydrology (Gray et al., 2005). The time separation between interferograms must be long enough to damp data noise due to the wet turbulent atmosphere; but long enough to include enough cumulative tidal

KIM ET AL. 2 of 10

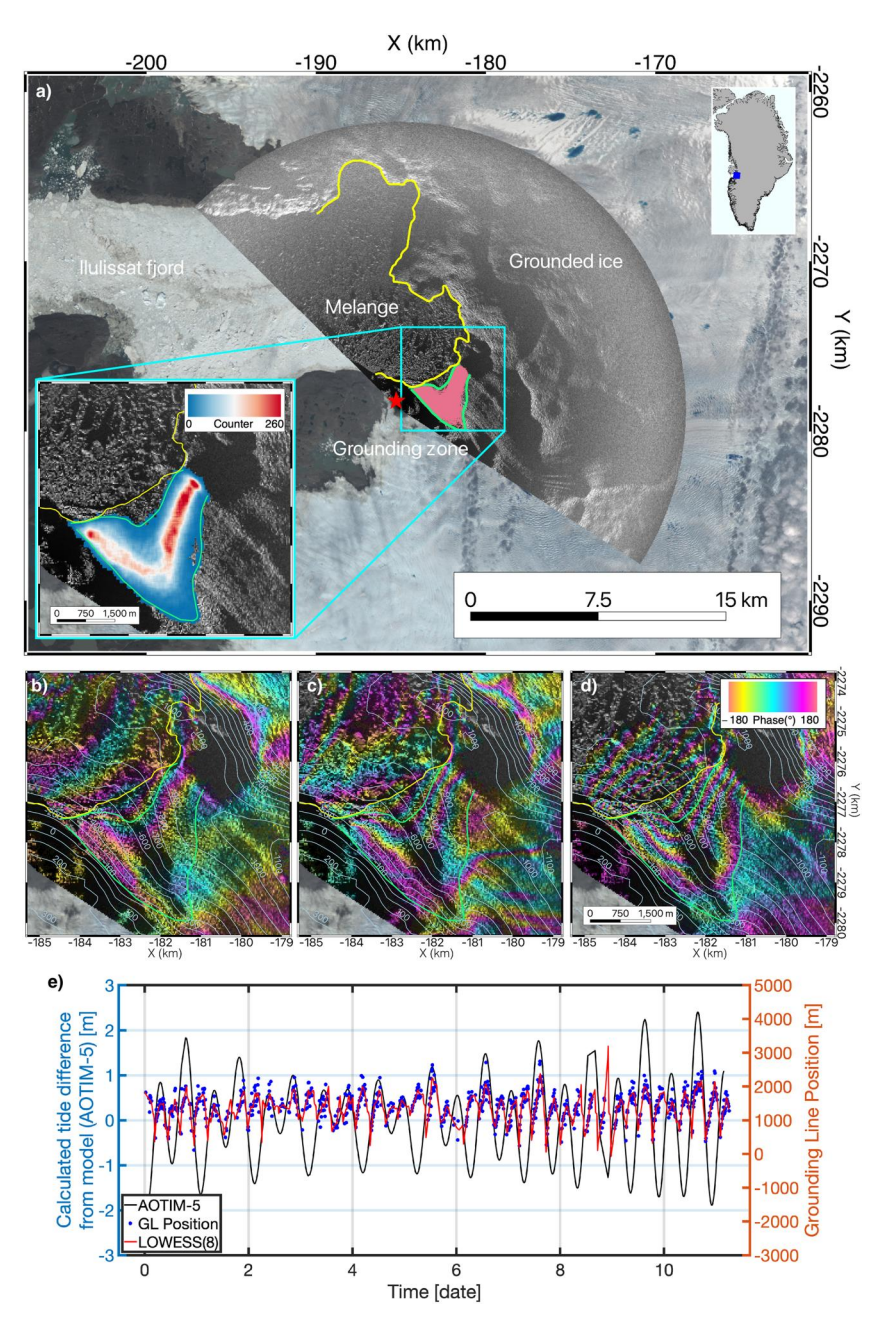


Figure 1. Survey of Jakobshavn Isbræ, Greenland with GPRI in June 2016 with the (a) GPRI radar intensity image overlaid on a Landsat-8 image (13 June 2016) with the GPRI instrument location at the red star. Ice front (yellow), grounding zone (green), grounding lines (pink), and a histogram of the grounding line position (enlarged cyan box). Double difference interferograms corresponding to the (b) most advanced grounding line position (P1 in Figure 2), (c) in between position (P2 in Figure 2) and (d) most retreated position (P3 in Figure 2). The color-coded interferometric phase is overlaid on the radar intensity image. Every color cycle in panels (c)–(d) is a 360° change in phase, equivalent to a 9 mm incremental motion of the ice surface toward the radar looking direction. (e) position of the grounding line along profile C–C' (see Figure 3) against time (blue dots) and differential tide signal calculated from AOTIM-5 (thin black). Red curve is a smoothed version of the grounding line positions using 8 consecutive positions.

deformation, that is, a time separation of hours. With a dominant diurnal cycle of 12 hr, peak to peak variations in tidal displacement occur every 6 hr.

Here, we form radar interferograms using data acquired 16-min apart that we difference every 6 hr to maximize the detection of tidal signal (Figures S2–S3 in Supporting Information S1). We extend the analysis over 2 weeks. From

KIM ET AL. 3 of 10

19448007, 2024, 6, Downloaded from https://agupubs.onlinelibary.wiley.com/doi/10.1092/2023GL106181 by Test, Wiley Online Library on [03:04/2024]. See the Terms and Conditions (https://onlinelibrary.wiley.com/remrs-and-conditions) on Wiley Online Library for rules of use; OA articles are governed by the applicable Creative Commons License

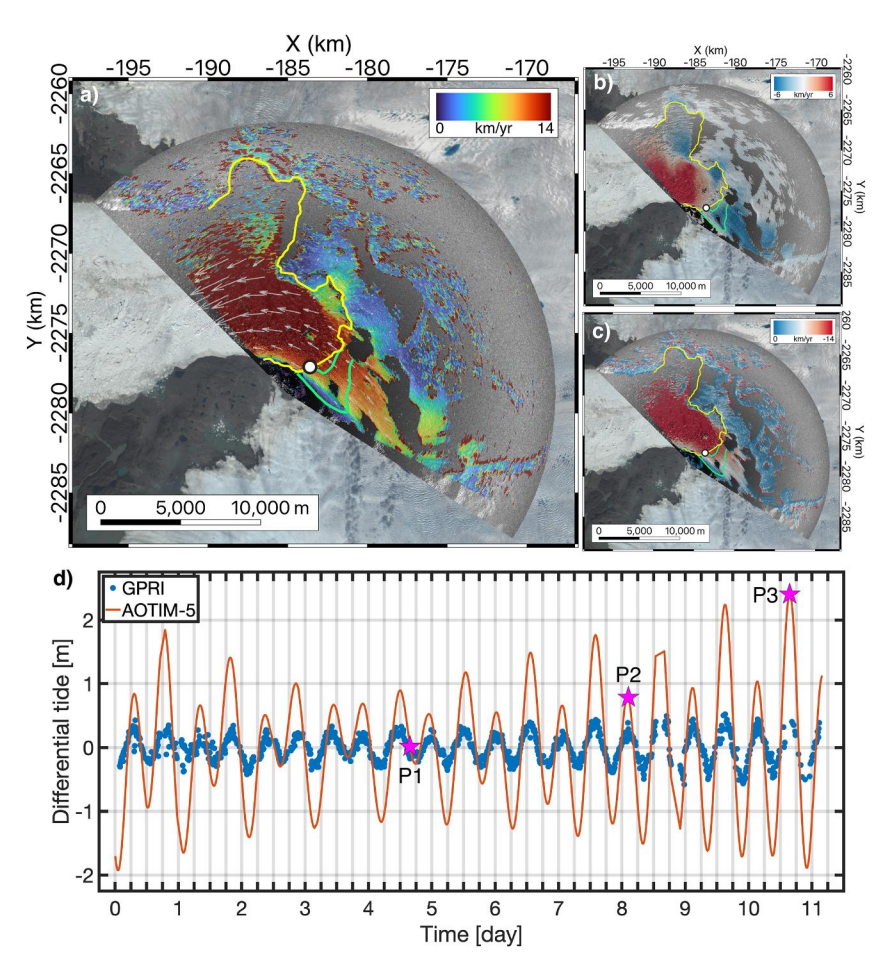


Figure 2. Velocity map and tidal motion of Jakobshavn Isbræ (a) ice speed in km/yr from speckle tracking in slant-range and azimuth overlaid on the radar intensity image and a Landsat-8 image; grounding zone is green and ice front is yellow, (b) geocoded ice speed in slant-range; and (c) azimuth (along scan) in km/yr. (d) differential motion at the white point in panels (a)–(c) in the zone of zero range motion converted into a vertical displacement (blue dots) versus the differential tidal amplitude over 6 hr from the AOTIM-5 model (red curve) in Ilulissat fjord in meters. P1, P2, and P3 correspond to zero tide difference (Figure 1b), medium tide difference (neap tide) (Figure 1c), and maximum tide difference (spring tide) (Figure 1d) interferograms, respectively.

the unwrapped differential interferograms, we locate the transition boundary where the ice surface is first displaced vertically, or first fringe, which is a proxy for the grounding line location (Rignot et al., 2011). By repeating the exercise over time, we measure how the grounding line migrates back and forth with changes in oceanic tide (Figures 1 and 2). The envelope of the grounding line positions defines what we refer to as the "grounding zone."

To quantify the variability in grounding line position, we count the number of times the grounding line crosses each cell of the geocoded interferogram. The distribution of counts (Figure 1a) is centered at mid-range and is broadly symmetric. The grounding zone envelope includes all of the inferred positions.

We compare the vertical displacements measured from interferometric data with the differential tidal displacement calculated using the AOTIM-5 tide model at 5 km resolution (Figure 2) (Padman & Erofeeva, 2004). The tidal range from the AOTIM-5 model is ± 1.4 m. To compare displacements in the vertical direction, the slant-range radar measurements are converted using the local incidence angle of the illumination based on radar look angle and surface topography.

2.4. Ice Surface Elevation

On average, the ice deviates from hydrostatic equilibrium by a few meters in the flexure zone due to bending stresses (Chartrand & Howat, 2023). In addition, the ice surface also deviates from flotation because flotation

KIM ET AL. 4 of 10

19448007, 2024, 6, Downloaded from https://agupubs.onlinelibrary.wiley.com/doi/10.1029/2023GL106181 by Test, Wiley Online Library on [03/04/2024]. See the Terms and Conditions (https://onlinelibrary.wiley.

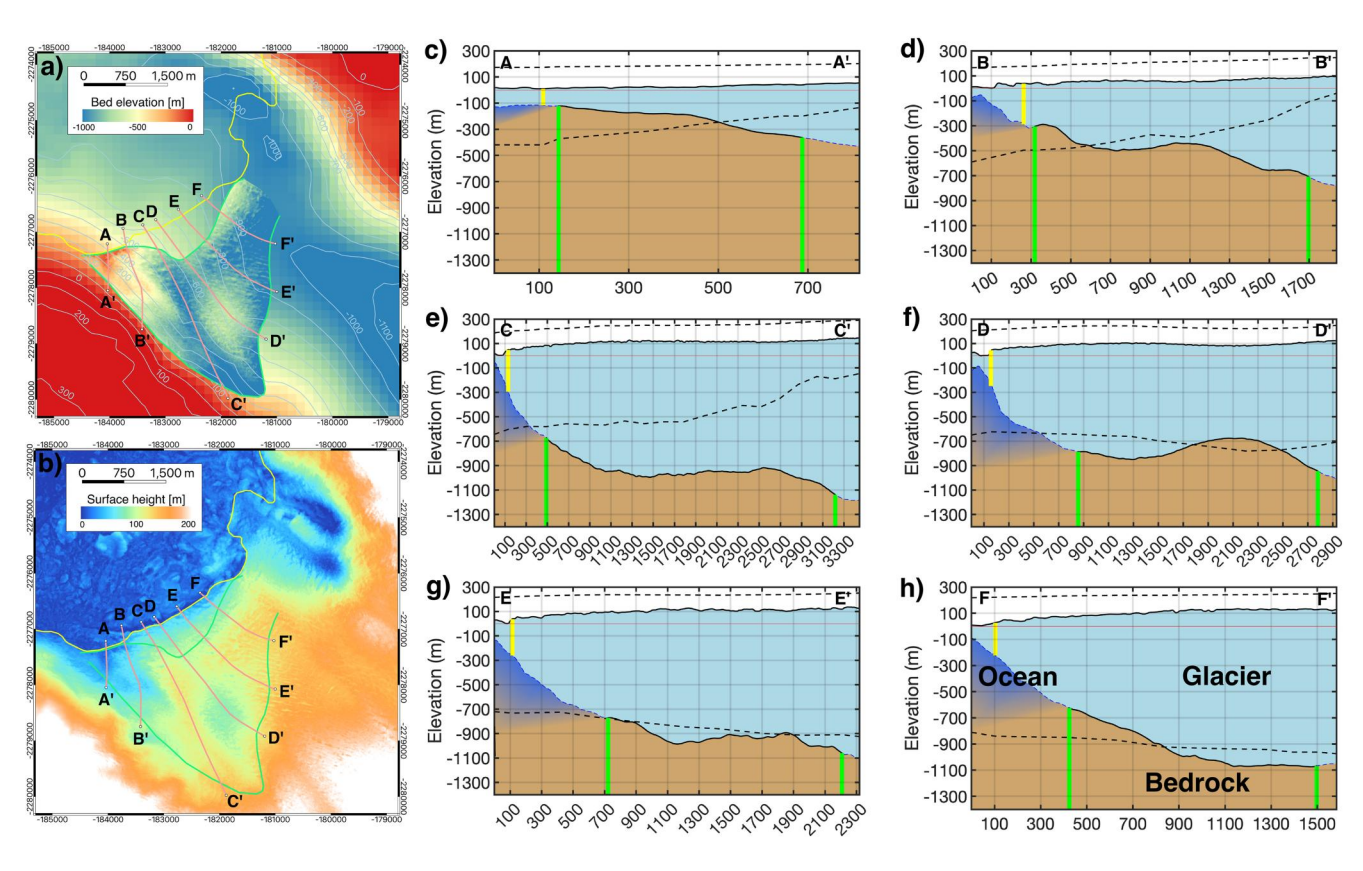


Figure 3. Bed elevation of Jakobshavn Isbræ (a) deduced from WV digital elevation model (DEM) within the grounding zone assuming flotation and overlaid on the BMv3 bed elevation and (b) surface height map from WV DEM. Green is the grounding zone. Yellow is the ice front. Pink lines are profiles (c-h) with surface elevation from the WV DEM (solid black line), BMv3 (dashed black line), and the new bed position from this study in between the grounding zone (solid black line) and outside of the grounding zone (blue dashed line). Yellow vertical solid line and green vertical solid lines in panels (c-h) indicate the ice front position and grounding zone positions, respectively. In front of grounding zones, water column is indicated as a blue color that blurs into brown with depth because we do not know the bed elevation.

applies on an average sense, at a scale of one ice thickness, and not at the scale of 10-100 m. Under this hypothesis, we calculate the bed depth necessary to maintain hydrostatic equilibrium of the ice surface using the density of ice, 917 kg/m^3 , and seawater, $1,028 \text{ kg/m}^3$. We assume that bridging effects are negligible (Van Der Veen & Whillans, 1989; Yu et al., 2017). For the surface reference, we use a World View digital elevation model (DEM) acquired on 16 June 2016, coincident with the GPRI data. The vertical precision of the DEM is 1 m at 2 m posting.

2.5. Range and Azimuth Displacements

We calculate ice motion in vector form using image offsets calculated in slant-range (line of sight) and azimuth (along-scan) using the ampcor algorithm (Rosen et al., 2004) with image pairs separated by 3 hr (Figure S4 in Supporting Information S1). The range spacing is 0.75 versus 4 m–54 m in azimuth from near to far range, respectively. The precision of speckle tracking in range is 10 times less than the interferometric phase (Mouginot, Scheuchl, & Rignot, 2019), but the ice motion is measured in vector form from the combination of range and azimuth displacements. We employ image chips of 64 elements in range pixels by 16 elements in azimuth, and a search window of 16×16 in the 1-look image data. Data noise is reduced from the image offsets using a median filter. We combine and filter the results over 2 weeks to get a reference velocity map, which includes the ice mélange (Figure 2). The results are geocoded at 30 m and translated into a velocity vector map in east and north directions after correction for the look angle of the radar.

In the slant-range displacement map, we delineate the region where ice moves perpendicular to the line of sight, that is, range displacements average zero. This band crosses the glacier ice front. In that region, the short-term phase signal, if any, cannot detect changes in horizontal motion because the motion remains perpendicular to the line of sight. We will only sense vertical displacements in that region. We use it to verify that the phase signal

KIM ET AL. 5 of 10

Geophysical Research Letters

10.1029/2023GL106181

observed in the differential interferograms is not associated with a change in horizontal motion of the glacier but to a vertical (tidal) motion.

We use the vector velocity map, which yields strain rates and flow direction, to estimate the buttressing force exerted by the ice mélange in front of the glacier onto the glacier front. The mélange is cohesive during the time of imaging because it remains coherent to the radar, and we find no fault zones in the phase map or abrupt transitions. We treat the mélange as a solid floating ice shelf unit. The WV DEM provides precise data about the ice mélange surface elevation, and in turn its ice thickness since it is in full hydrostatic equilibrium. A number of studies have attributed a role to the ice mélange in controlling iceberg calving (Cassotto et al., 2021; Xie et al., 2019).

2.6. Bathymetry

We use BedMachine Greenland Version 3.0 (BMv3) (Morlighem et al., 2017b), which incorporates multibeam echosounder data, discrete soundings, and gravity inversions (An et al., 2017).

3. Results

3.1. Tidal Signal

Along the zone of glacier flow that moves perpendicular to the radar line of sight, that is, the radar cannot sense horizontal ice motion and changes in horizontal motion, we observe a cyclic displacement, in phase with the tidal difference, consistent with a vertical motion induced by changes in oceanic tide, but of reduced amplitude (Figure 2). We conclude that the differential displacements observed in the differential interferograms capture the glacier tidal motion.

The typical range of vertical motion is ±50 cm on grounded ice vs. a peak to peak tidal signal of 2.8 m. The reduced range of variability on grounded ice is consistent with ice being partially afloat. The ice surface lifts up at high tide, allowing seawater to intrude beneath the glacier ice. The ice surface moves back down at low tide, forcing seawater to extrude from the cavity beneath grounded ice. We highlight two differential interferograms: (a) P1 at a minimum tidal difference, and (b) P3 at a maximum tidal difference during spring tide (Figures 1 and 2). The corresponding interferograms reveal the minimum and maximum positions of the grounding line during the tidal cycle, respectively (Figures 1b and 1d). The maximum distance between grounding line positions is 2.8 km at the glacier center.

In the ice mélange, we cannot unwrap the interferometric phase from a zone of zero displacement because the tidal motion is too large to avoid phase aliasing, and the motion of the sea ice mélange mixes horizontal, rotational, tilt, rifting, faulting, and vertical motions.

3.2. Grounding Line Positions

We detect a grounding line only on the south side of the glacier. The north side is in the shadow of the radar, due to a depression in surface topography, which indicates that ice is thin in that sector. The spatial pattern of ice deformation matches what we expect from the visco-elastic deformation of glacier ice in a flexure zone, for example, a step-wise, regular pattern of interferometric fringes across the glacier width, with a consistent number of fringes across the glacier, regularly spaced (Rignot et al., 2011). A change in horizontal speed would exhibit a different pattern of interferometric fringes, analog to the pattern of fringes for horizontal motion, which is higher in the middle than on the sides. A change in horizontal motion would not yield a pattern of regularly spaced fringes. Again, the motion measured with differential interferometry is thus mainly caused by vertical motion.

Since we difference interferograms 6 hr apart, the tide difference ranges from a maximum negative tide difference (red dots in Figure S5 in Supporting Information S1, low peaks in Figure 1e) to a maximum positive tide difference (blue dots in Figure S5 in Supporting Information S1, high peaks in Figure 1e). The negative tide difference maximum means a low tide minus a high tide whereas the positive tide difference maximum means a high tide minus a low tide (e.g., -1m - (+1m) = -2m, and +1m - (-1m) = +2m). The grounding line migrates to an upstream position as the absolute magnitude of the tide difference increases and migrates to the ice front when the tide difference drops to zero (Figure 1e and Figure S5b in Supporting Information S1) (Movie S1).

KIM ET AL. 6 of 10

3.3. Grounding Zone

By repeating the measurements over several tidal cycles, we delineate the envelope of grounding line positions or "grounding zone." The grounding zone varies from a few hundred meters in width on the southern flank to 2.8 km at the center and drops down to zero toward the north. The interferogram with the most upstream position (P3 in Figure 2) corresponds to the highest differential positive tide, at spring tide. Conversely, the most advanced position of the grounding line (P1 in Figure 2) corresponds to a near zero differential tide. In between, the grounding line migrates smoothly between these end positions (Figure 1).

3.4. Bed Depth in the Grounding Zone

Using the WV DEM, we deduce the minimum glacier depth in the grounding zone that is compatible with flotation. We find that the bed must be 100–800 m deeper than in BMv3 to make ice flotation possible. In a few places, for example, along the flanks of the GZ, the bed estimates are slightly lower than BMv3, but by large the calculation reveals a deeper bed than previously known, with a deep channel (labeled C–C') along the center of the southern side where the grounding zone is the widest and bed elevation is 300 m deeper than in BMv3 (Figure 3d).

We compare the range of grounding line migration with the inferred bed slope (Note that surface and bed slopes are herein linearly related). A positive bed slope is a prograde slope, where bed elevation increases from the ice front to the upstream regions. A negative bed slope is a retrograde slope, where the bed elevation decreases from the ice front to the upstream regions. The results show a strong positive correlation between grounding zone width and bed slope. We considered linear (1 degree of freedom) and exponential (2 degree of freedom) fit to the data. We find that exponential yields a lower χ^2 value and a higher R^2 value (Table S2 in Supporting Information S1). A quasi-exponential dependence is expected in the context of a visco-elastic beam deforming on an elastic bed (Sayag & Worster, 2011). Narrow grounding zone width occur on bed slopes with pronounced spatial variations, which is consistent with more complex pathways for water intrusions. Wider grounding zone widths occur with shallower bed slopes, that is, bed channels like C-C' (Figure S6 in Supporting Information S1), which is consistent with intrusions along open pathways over long distances.

3.5. Horizontal Motion Versus Tide

The noise level in areas of no flow (i.e., grounded ice) is 25 m/yr or 0.07 m/day in the slant-range direction and 25 m/yr or 0.07 m/day in the azimuth direction. After geocoding and correction for the low grazing angle of the radar, the error increases to 140 m/yr or 0.4 m/day in both the x- (easting) and y- (northing) directions. The error in flow direction, which is the error in velocity divided by two times the mean velocity (Mouginot et al., 2012), is 0.7° for a glacier speed of 12 km/yr. The map of ice motion from speckle tracking is therefore precise enough to give us the flow direction within 1°. Over 12 days, all tidal aliases average out. We detect flow speeds of 14 km/yr near the ice front, increasing to 19 km/yr in the ice mélange. The flow vectors from speckle tracking align well with the flow line visible as perturbations of the glacier surface (Figure S4 in Supporting Information S1).

In the region flowing perpendicular to the radar illumination, the line of sight speed averages zero over several cycles, within errors (i.e., 0.1 m/day), as expected. When we examine details in the line of sight speed during the tidal cycle in that region, we detect a motion in phase with the tidal difference within the grounding zone and no motion outside of the grounding zone (Figure 2). This signal is therefore consistent with ice within the grounding zone moving vertically with changes in oceanic tide.

3.6. Buttressing Force

We use the ice motion recorded in front of JI to calculate the buttressing force exerted by the mélange on the glacier (Rignot, 2001; Thomas, 2004). The transition from glacier ice to the mélange is a continuum, as shown by the thickness profile in Figure 3. The backpressure, F, exerted by a floating ice shelf is, $F = 0.5\rho_i ghH - 2H\bar{B}\dot{c}_x^{1/3}$. The first term of the expression of F is the action of sea-water pressure, where $\rho_i = 917 \text{ kg/m}^3$, g is the acceleration of gravity (9.81 cm/s²), h is the mélange surface elevation above sea level from the WV DEM, and H is the ice thickness deduced from hydrostatic equilibrium using a seawater density of 1,028 kg/m³. The second term of the expression of F is the action of the ice mélange longitudinal spreading, where \bar{B} is the temperature-dependent deformation constant of ice in kPa/yr^{1/3}, and \dot{c}_x is the longitudinal spreading rate of ice (x-axis aligned with

KIM ET AL. 7 of 10

the flow direction, positive $\dot{\varepsilon}_x$ means extensional flow) in units of per year. We assume a Glen's flow law with an exponent of n=3. In this framework, we assume that the transition from glacier to mélange is a continuum. Over most of the ice front, the ice thickness inferred from flotation drops only slowly in the along flow direction (Figure 3), so this is a reasonable assumption.

We calculate \dot{e}_x over a length scale of 1–2.8 km along flow lines initiated at the ice front across the entire glacier front. We use average values of h and H along each 1–2.8 km long profiles to calculate F (Table S1 in Supporting Information S1). We find that h averages 16 ± 5 m, H averages 134 ± 40 m, and \dot{e}_x averages 0.7 ± 0.8 /yr and is never negative. In the presence of cold ice, \bar{B} would be about 500 kPa/yr^{1/3}, but here the mélange is close to its melting point, so we use $\bar{B} = 100$ kPa/yr^{1/3}. Higher values of \bar{B} would make F negative, which is not physically possible. We calculate a buttressing force, F, that averages -9 ± 16 MN/m (Mega Newton per meter), that is, not significantly different from zero compared with the other glaciers, for example, 812 MN/m for Pine Island Glacier, 110 MN/m for Thwaites Glacier, and 1540 MN/m for Rutford Ice Stream (Rignot, 2001). We conclude that the buttressing of the ice mélange in front of JI is negligible at the time of imaging of the glacier.

4. Discussion

Although GPRI data have been analyzed before, including the pattern of ice motion with tide (Cassotto et al., 2021; Voytenko et al., 2015; Xie et al., 2019), it is the first time to the best of our knowledge that differential interferometry has been used to examine tidal motion. A number of studies have revealed that the horizontal motion of a marine-terminating glacier may be modulated by changes in ocean tide (Voytenko et al., 2015). In the case of JI, the examination of the zone of flow perpendicular to the horizontal motion, the pattern of deformation, and its spatial extent are indicative of pure tidal motion and no change in horizontal speed with the tide. Using these double difference data, we detect a large migration of the grounding line with tide.

The migration reveals kilometer-scale seawater intrusions beneath grounded ice. There are no other physical phenomena that explains the uplift of the ice surface in phase with the tidal difference other than water intrusion. The height of the deflection is a proxy for the thickness of the water layer. The thickness is smaller than the tidal amplitude and in the range of ± 30 cm on the south side (Figure 1) and zero elsewhere, that is, the remainder of the terminus is grounded.

The level of grounding line migration (1–2.8 km) over 6 hr implies a rate of cavity opening of 5–12 cm/s, which is significant in terms of entrainment speed of ocean water along basal ice. The rate of basal melt is proportional to the entrainment speed of seawater. We expect intrusions to cause vigorous melt. Extrusions might be less efficient due to heat loss in the cavity and melt water to be trapped at low tide (Warburton et al., 2020). Melting of basal ice at a grounding zone is not included in models at present, but prior simulations indicate that including them in a kilometer-size grounding zone significantly increases the projections of sea level rise (Robel et al., 2022; Seroussi & Morlighem, 2018).

Increasing melt rates of basal ice in the grounding zone, for example, due to warmer ocean waters, will reduce basal friction over a considerable area instead of a fixed grounding line. If the ice removal rate is strong enough, that is, faster than the rate of ice replenishment from upstream, the glacier will un-ground from its bed, and retreat. The glacier retreat may facilitate ice shelf regrowth to counteract the retreat. Yet overall, the seawater intrusions will enhance the sensitivity of the glacier to ocean thermal forcing.

The discrepancy between our bed estimates and BMv3 illustrate the high degree of uncertainty that remains in the determination of bed topography and ice thickness of JI. The 4-m accuracy of World View DEM without ground control points, yields an uncertainty in bed elevation of 33 m. While errors in bed mapping of 100 m are common in areas with few direct measurements (e.g., radar sounding data or multibeam echo sounding), the errors reported herein exceed 100 m, for example, along C–C′. The uncertainty of bridging stresses is about 1–2 m in surface elevation and 10–20 m in thickness, hence much smaller than the errors reported here (Van Der Veen & Whillans, 1989; Yu et al., 2017). We attribute the error in prior bed mapping to a lack of direct measurements of ice thickness from depth radar sounders, errors in flow direction measured with satellites, uncertainties in corrections for ice thinning, and a lack of depth data at the ice front. More surveys are needed to gain confidence in the bed topography of the lower reaches of JI.

KIM ET AL. 8 of 10



Acknowledgments

This work was performed in the

Department of Earth System Science.

University of California Irvine, and at

Caltech's Jet Propulsion Laboratory under

a contract with the National Aeronautics

and Space Administration as part of the

Greenland and with the NASA Earth and

Earth Venture Mission Ocean Melting

Space Science FINESST Fellowship

Program (Grant 80NSSC21K1620).

Geophysical Research Letters

10.1029/2023GL106181

A deeper glacier bed implies that thermal forcing from the ocean is greater due to the pressure dependence of the melting point of ice. For instance, a bed depth at 900 versus 800 m, increases the ocean thermal forcing by 0.25 °C. The strong vertical gradient in temperature observed in the fjord waters also implies warmer ocean waters at 900 m depth (Khazendar et al., 2019).

The ice mélange speeds up from 12 km/yr at the ice front to 19 km/yr over the course of 5 km (Figure S4 in Supporting Information S1). In winter, the mélange may suppress the rotation of ice blocks that detach into icebergs, which may change the longitudinal strain rates, and reduce glacier speed. In summer, the mélange is presumed not to have a significant influence (Amundson et al., 2010; Joughin et al., 2008). At the time of our radar imaging, that is, late spring, with bergs stranded in front of the glacier among thick, cohesive mélange, we calculate that the mélange exerts no buttressing.

While the data herein refer to JI, other small floating extensions exist in Greenland, for example, on Rink, Alison, Ryder, Steensby, Humboldt, and larger ones on Petermann, 79north, Zachariae, Storstrommen, Ostenfeld, Hagen Brae (Wood et al., 2021). Seawater intrusions have been revealed by satellite radar interferometry on Petermann Glacier where the grounding zone width exceeds 6 km (Ciracì et al., 2023). Many other glaciers are likely to experience seawater intrusions if their ice fronts are near flotation (Wilson et al., 2020). The impact of these intrusions on glacier stability ought to be studied in more detail. Seawater intrusions will make the glaciers more sensitive to ocean warming and in turn increase the projections of mass loss from these glaciers (Ciracì et al., 2023; Robel et al., 2022).

5. Conclusions

Using data acquired every 2 min, we map the grounding line of JI for the first time, at a high precision, and detect its migration in phase with changes in oceanic tide. The grounding line migrates over many kilometers, which we attribute to seawater intrusion beneath grounded ice. The grounding zone is up to 2.8 km in width, which is 10 times wider than expected from hydrostatic equilibrium, because the bed geometry needs updating. The results imply that the glacier bed elevation ought to be much deeper than expected. In addition, the results suggest that seawater intrusions will move at high speed and may therefore melt basal ice vigorously. These findings are of relevance to the modeling of glacier evolution because a deeper bed and a more vigorous ocean heat exchange at the glacier base will make the glacier more sensitive to ocean warming than previously recognized.

Data Availability Statement

The GPRI differential interferograms, grounding lines, grounding zone, velocity maps, and DEMs are posted on the dryad web site at UCI (Kim et al., 2023). BedMachine is available at (Morlighem et al., 2017a).

References

Amundson, J. M., Fahnestock, M., Truffer, M., Brown, J., Lüthi, M. P., & Motyka, R. J. (2010). Ice mélange dynamics and implications for terminus stability, Jakobshavn Isbræ, Greenland. *Journal of Geophysical Research*, 115(F1). https://doi.org/10.1029/2009jf001405

An, L., Rignot, E., Elieff, S., Morlighem, M., Millan, R., Mouginot, J., et al. (2017). Bed elevation of Jakobshavn Isbræ, West Greenland, from high-resolution airborne gravity and other data. *Geophysical Research Letters*, 44(8), 3278–3736. https://doi.org/10.1002/2017gl073245

Cassotto, R., Burton, J., Amundson, J., Fahnestock, M., & Truffer, M. (2021). Granular decoherence precedes ice mélange failure and glacier calving at Jakobshavn Isbræ. *Nature Geoscience*, 14(6), 417–422. https://doi.org/10.1038/s41561-021-00754-9

Chartrand, A. M., & Howat, I. M. (2023). A comparison of contemporaneous airborne altimetry and ice-thickness measurements of Antarctic ice shelves. *Journal of Glaciology*, 1–14. https://doi.org/10.1017/jog.2023.49

Ciracì, E., Rignot, E., Scheuchl, B., Tolpekin, V., Wollersheim, M., An, L., et al. (2023). Melt rates in the kilometer-size grounding zone of Petermann Glacier, Greenland, before and during a retreat. *Proceedings of the National Academy of Sciences of United States of America*, 120(20). https://doi.org/10.1073/pnas.2220924120

Clarke, T. S., & Echelmeyer, K. (1996). Seismic-reflection evidence for a deep subglacial trough beneath Jakobshavns Isbræ, West Greenland. Journal of Glaciology, 43(141), 219–232. https://doi.org/10.1017/s0022143000004081

Derkacheva, A., Mouginot, J., Millan, R., Maier, N., & Gillet-Chaulet, F. (2020). Data reduction using statistical and regression approaches for ice velocity derived by landsat-8, sentinel-1 and sentinel-2. *Remote Sensing*, 12(12), 1935. https://doi.org/10.3390/rs12121935

Fenty, I., Willis, J. K., Khazendar, A., Dinardo, S., Forsberg, R., Fukumori, I., et al. (2016). Oceans Melting Greenland: Early results from NASA's ocean-ice mission in Greenland. *Oceanography*, 29(4), 72–83. https://doi.org/10.5670/oceanog.2016.100

Friedl, P., Weiser, F., Fluhrer, A., & Braun, M. (2020). Remote sensing of glacier and ice sheet grounding lines: A review. *Earth-Science Reviews*, 201, 102948. https://doi.org/10.1016/j.earscirev.2019.102948

Gray, L., Joughin, I., Tulaczyk, S., Spikes, V. B., Bindschadler, R., & Jekek, K. (2005). Evidence for subglacial water transport in the West Antarctic Ice Sheet through three-dimensional satellite radar interferometry. *Geophysical Research Letters*, 32(3), L03501. https://doi.org/10. 1029/2004eJ021387

1027/2401gl(21307

KIM ET AL. 9 of 10

- Holland, D. M., Thomas, R. H., De Young, B., Ribergaard, M. H., & Lyberth, B. (2008). Acceleration of Jakobshavn Isbrae triggered by warm subsurface ocean waters. *Nature Geoscience*, 1(10), 659–664. https://doi.org/10.1038/ngeo316
- Joughin, I., Abdalati, W., & Fahnestock, M. A. (2004). Large fluctuations in speed on Greenland's Jakobshavn Isbræ glacier. Nature, 432(7017), 608–610. https://doi.org/10.1038/nature03130
- Joughin, I., Howat, I. M., Fahnestock, M., Smith, B., Krabill, W., Alley, R. B., et al. (2008). Continued evolution of Jakobshavn Isbrae following its rapid speedup. *Journal of Geophysical Research*, 113(F4). https://doi.org/10.1029/2008jf001023
- Khazendar, A., Fenty, I. G., Carroll, D., Gardner, A., Lee, C. M., Fukumori, I., et al. (2019). Interruption of two decades of Jakobshavn Isbrae acceleration and thinning as regional ocean cools. *Nature Geoscience*, 12(4), 277–283. https://doi.org/10.1038/s41561-019-0329-3
- Kim, J. H., Rignot, E., Holland, D., & Holland, D. (2023). Data for: Seawater intrusion at the grounding line of Jakobshavn Isbrae, Greenland, from terrestrial radar interferometry (tri) [dataset]. Dryad. https://doi.org/10.5061/dryad.1c59zw423
- Leuschen, C., Gogineni, P., Rodriguez-Morales, F., Paden, J., & Allen, C. (2010). *IceBridge MCoRDS L2 ice thickness*, 2002–2017. NASA DAAC at the National Snow and Ice Data Center.
- Morlighem, M., Williams, C., Rignot, E., An, L., Arndt, J. E., Bamber, J., et al. (2017a). Icebridge bedmachine Greenland, version 3 [dataset]. NASA National Snow and Ice Data Center Distributed Active Archive Center. https://doi.org/10.5067/2CIX82HUV88Y
- Morlighem, M., Williams, C. N., Rignot, E., An, L., Arndt, J. E., Bamber, J. L., et al. (2017b). Bedmachine v3: Complete bed topography and ocean bathymetry mapping of Greenland from multibeam echo sounding combined with mass conservation. *Geophysical Research Letters*, 44(21), 11051–11061. https://doi.org/10.1002/2017g1074954
- Mouginot, J., Rignot, E., Bjørk, A. A., van den Broeke, M., Millan, R., Morlighem, M., et al. (2019). Forty-six years of Greenland Ice Sheet mass balance from 1972 to 2018. *Proceedings of the National Academy of Sciences of United States of America*, 116(19), 9239–9244. https://doi.org/10.1073/pnas.1904242116
- Mouginot, J., Scheuchl, B., & Rignot, E. (2012). Mapping of ice motion in Antarctica using Synthetic-Aperture Radar Data. *Remote Sensing*, 4(9), 2753–2767. https://doi.org/10.3390/rs4092753
- Mouginot, J., Scheuchl, B., & Rignot, E. (2019). Continent-wide, interferometric SAR phase, mapping of Antarctic ice velocity. Geophysical Research Letters, 46(16), 9710–9718. https://doi.org/10.1029/2019gl083826
- Padman, L., & Erofeeva, S. (2004). A barotropic inverse tidal model for the Arctic Ocean. Geophysical Research Letters, 31(2). https://doi.org/10.1029/2003gl019003
- Rignot, E. (1996). Tidal motion, ice velocity and melt rate of Petermann Gletscher, Greenland, measured from radar interferometry. *Journal of Glaciology*, 42(142), 476–485. https://doi.org/10.3189/s0022143000003464
- Rignot, E. (2001). Evidence for rapid retreat and mass loss of Thwaites Glacier, West Antarctica. Journal of Glaciology, 106(157), 213–222. https://doi.org/10.3189/172756501781832340
- Rignot, E., Mouginot, J., & Scheuchl, B. (2011). Antarctic grounding line mapping from differential satellite radar interferometry. *Geophysical*
- Research Letters, 38(L10504), 1–6. https://doi.org/10.1029/2011gl047109

 Robel, A., Wilson, E., & Seroussi, H. (2022). Layered seawater intrusion and melt under grounded ice. The Cryosphere, 16(2), 451–469. https://
- doi.org/10.5194/tc-16-451-2022
 Rosen, P., Hensley, S., Peltzer, G., & Simons, M. (2004). Updated repeat orbit interferometry package released. *Eos, Transactions American*
- Geophysical Union, 85(5), 47. https://doi.org/10.1029/2004eo050004

 Rosenau, R., Schwalbe, E., Maas, H.-G., Baessler, M., & Dietrich, R. (2013). Grounding line migration and high-resolution calving dynamics of
- Jakobshavn Isbræ, West Greenland. Journal of Geophysical Research: Earth Surface, 118(2), 382–395. https://doi.org/10.1029/2012jf002515 Sayag, R., & Worster, M. G. (2011). Elastic response of a grounded ice sheet coupled to a floating ice shelf. Physical Review E - Statistical
- Physics, Plasmas, Fluids, and Related Interdisciplinary Topics, 84(3), 036111. https://doi.org/10.1103/physreve.84.036111
 Seroussi, H., & Morlighem, M. (2018). Representation of basal melting at the grounding line in ice flow models. The Cryosphere, 12(10), 3085–3096. https://doi.org/10.5194/tc-12-3085-2018
- Thomas, R. H. (2004). Force-perturbation analysis of recent thinning and acceleration of Jakobshavn Isbræ, Greenland. *Journal of Glaciology*, 50(168), 57–66. https://doi.org/10.3189/172756504781830321
- Thomas, R. H., Frederick, E., Krabill, W., Manizade, S., & Martin, C. (2009). Recent changes on Greenland outlet glaciers. *Journal of Glaciology*,
- 55(189), 147–162. https://doi.org/10.3189/002214309788608958

 Van Der Veen, C., & Whillans, I. (1989). Force budget: I. Theory and numerical methods. *Journal of Glaciology*, 35(119), 53–60. https://doi.org/
- 10.3189/002214389793701581

 Voytenko, D., Stern, A., Holland, D. M., Dixon, T. H., Christianson, K., & Walker, R. T. (2015). Tidally driven ice speed variation at Helheim Glacier, Greenland, observed with terrestrial radar interferometry. *Journal of Glaciology*, 61(226), 301–308. https://doi.org/10.3189/
- Warburton, K., Hewitt, D., & Neufeld, J. (2020). Tidal grounding-line migration modulated by subglacial hydrology. *Geophysical Research Letters*, 47(17), e2020GL089088. https://doi.org/10.1029/2020gl089088
- Werner, C., Strozzi, T., Wiesmann, A., & Wegmüller, U. (2008). Gamma's portable radar interferometer. In *Proceedings of 13th FIG Symposium on Deformation Measurement and Analysis* (pp. 1–10).
- Wilson, E., Wells, A. J., Hewitt, I. J., & Cenedese, C. (2020). The dynamics of a subglacial salt wedge. *Journal of Fluid Mechanics*, 895, A20. https://doi.org/10.1017/jfm.2020.308
- Wood, M., Rignot, E., Bjørk, A. A., van den Broeke, M., Fenty, I., Menemenlis, D., et al. (2021). Ocean forcing drives glacier retreat in Greenland. Science Advances, 7(1), eaba7282. https://doi.org/10.1126/sciadv.aba7282
- Xie, S., Dixon, T., Holland, D., Voytenko, D., & Vankova, I. (2019). Rapid iceberg calving following removal of tightly packed pro-glacial mélange. Nature Communications, 10(3250), 3250. https://doi.org/10.1038/s41467-019-10908-4
- Xie, S., Dixon, T., Voytenko, D., Deng, F., & Holland, D. (2018). Grounding line migration through the calving season at Jakobshavn Isbrae, Greenland, observed with terrestrial radar interferometry. *The Cryosphere*, 12(4), 1387–1400. https://doi.org/10.5194/tc-12-1387-2018
- Yu, H., Rignot, E., Morlighem, M., & Seroussi, H. (2017). Iceberg calving of Thwaites glacier, west Antarctica: Full-stokes modeling combined with linear elastic fracture mechanics. *The Cryosphere*, 11(3), 1283–1296. https://doi.org/10.5194/tc-11-1283-2017

KIM ET AL. 10 of 10